Electrochemical Insight into Na_xCoO_2 for the Oxygen Evolution Reaction and the Oxygen Reduction Reaction

Shaowei Song, Yaqin Wang, Ryan C. Davis, Zhensong Ren, Xin Xiao, Guang Yang, Dezhi Wang, Jiming Bao, Qinyong Zhang,* Shuo Chen,* and Zhifeng Ren*

ACCESS | Metrics & More | Article Recommendations | SI Supporting Information

ABSTRACT: Layered Na_xCoO_2 provides multiple degrees of freedom for manipulating its structure and physical properties by tuning the Na concentration, leading to specific functionalities including thermoelectricity, superconductivity, and potentiality in Li-/Na-ion batteries. However, the contribution of varied Na to charge transfer, electrocatalytic kinetics, and energetics in terms of the electrochemical interface reaction for the oxygen evolution reaction (OER) in water splitting and the oxygen reduction reaction (ORR) in fuel cells is not yet fully understood. This work reveals that varied Na concentrations indirectly affect the electrochemical OER or ORR activity by changing the Co–O bond in the constituent CoO_6 octahedron of Na_xCoO_2. Tuning the Na concentration gives rise to the unique evolution of the electronic configuration and subsequently further enhances the Co–O bond's covalency, which results in promoting the catalytic kinetics of OER and ORR. As the Fermi level descends deeper into the O 2p orbitals with increasing Na extraction, the lattice oxygen becomes active in the proton–electron transfer process, which is reflected in the pH and oxygen-concentration dependence of the OER activity. Based on the characterization of its electrochemical properties, the high electrocatalytic activity of $Na_{0.75}CoO_2$, which exhibits competent OER activity superior to that of IrO_2, is rationalized. Meanwhile, intrinsic $Na_{0.75}CoO_2$ reveals a half-wave potential of $0.74V_{RHE}$ for ORR. The evolution of the structure and the electronic configuration of Na_xCoO_2 related to its electrochemical properties enables further improved Na_xCoO_2-based catalysts for efficient electrochemical OER and ORR.
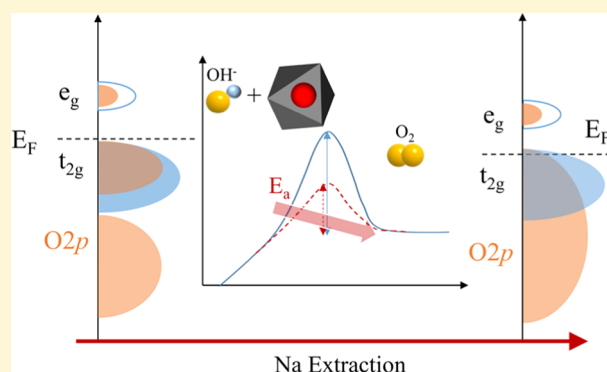
INTRODUCTION

Seeking highly efficient and stable catalysts for the oxygen evolution reaction (OER) and the oxygen reduction reaction (ORR) for alternative renewable energy has continued to be a critical challenge.[1−3] Layered sodium cobaltite, Na_xCoO_2, has attracted significant attention in the past few decades due to its multiple particular functionalities, such as magnetism, super-conductivity, and use as a cathode in batteries and catalysts, as well as thermoelectricity in energy storage and conversion devices.[4−7] The crystal structure and magnetism of sodium cobaltite were first investigated by Jansen and Hoppe.[8,9] Figure 1a shows that its crystal structure consists of Na ionic layers and CoO_2 sheets alternately stacked along the c axis. This peculiar two-dimensional structure gives rise to unique ion and charge carrier transport in separated layers.[10] The Na ionic character and the large channels between layers enable Na-ion intercalation/deintercalation in sodium-ion batteries.[7] The CoO_2 layer comprising edge-sharing CoO_6 octahedra is mainly responsible for the charge carrier transport in Na_xCoO_2.[11] Meanwhile, the crystalline structure of Na_xCoO_2 is susceptible to the Na content. The different types of Na coordination,

including octahedral, tetrahedral, and prismatic environments, are formed corresponding to nonstoichiometric Na.[12,13]

In the past few decades, deep insight into the crystal structure and condensed matter physics of Na_xCoO_2 has been gained due to extensive research regarding its use in thermoelectricity and superconductivity.[14,15] It has been found that the filling degree of Na not only controls the carrier transport in the CoO_2 layers but also governs the average valence state of Co (Co^{3+} and Co^{4+}).[16] Co^{3+} generally displays fivefold degenerated electronic states with low spin, while the emerging Co^{4+} $3d(t_{2g})$ presents sixfold degeneracy due to Na deficiency.[14,17,18] Determination of the effects of varied electronic structures and their related crystalline structures and coordination changes on the electrochemical properties remains elusive. A recent study on OER/ORR of
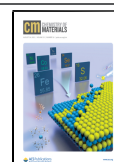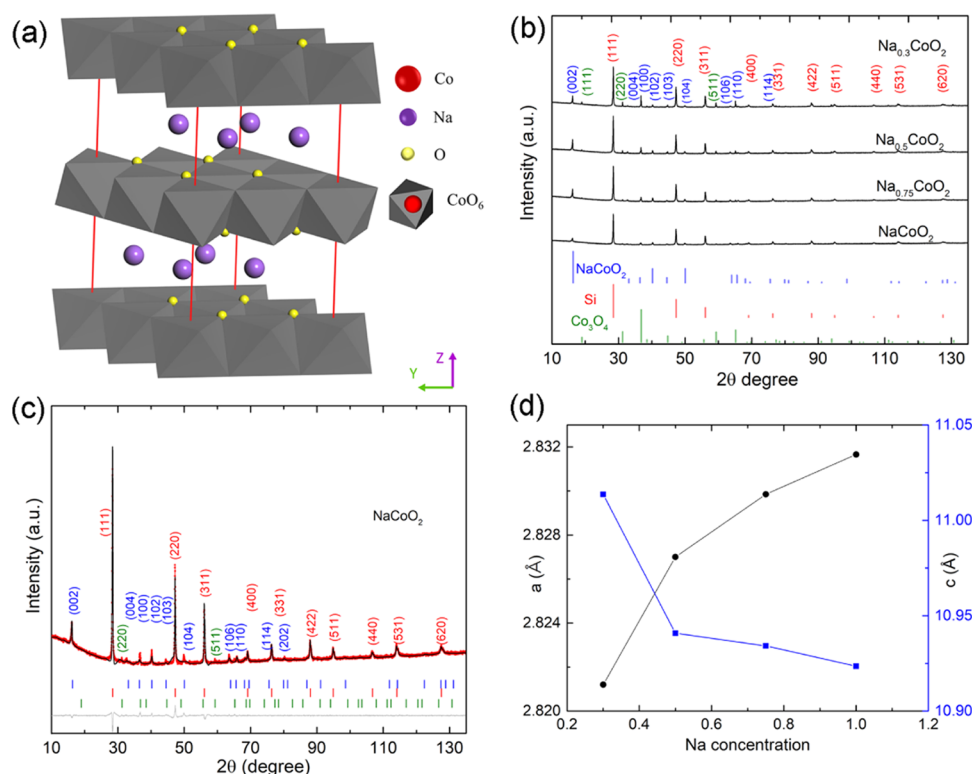
Figure 1. (a) Schematic illustration of the layered crystal structure of Na_xCoO_2. (b) XRD patterns of Na_xCoO_2 (x = 0.3, 0.5, 0.75, and 1) with $NaCoO_2$ PDF#27-0682, Si PDF#27-1402, and Co_3O_4 PDF#42-1467. (c) Rietveld refinement results for $NaCoO_2$. (d) Calculated lattice parameters a and c as functions of the Na concentration.

rutile and spinel oxides and perovskites has clarified that valence states and electronic structures could affect the intermediate steps, Gibbs free energy, and active sites in terms of the surface reaction mechanism.[19,20]

Co with octahedral coordination has played an influential role in OER/ORR in spinel oxides ($ZnCo_2O_4$, VCo_2O_4) and perovskites ($LaCoO_3$, $SrCoO_3$, $YBaCo_4O_{7+\delta}$).[21,22] Na_xCoO_2 is more advantageous in terms of the structure and transport in comparison with these spinel oxides and perovskites. As a layered structure, the layer thickness of the CoO_2 and Na_2O layers is dependent on the Na filling degree, which might be beneficial for obtaining a large exposed surface area for intermediates. Additionally, the excellent electronic conductivity necessary for decent OER/ORR catalysts can also be achieved by manipulating the Na concentration in Na_xCoO_2. The hole carriers are transported along the Co−O−Co chain in the a−b plane, which is established by the short distance between neighboring Co atoms and the overlapping of the Co 3d orbitals. Goodenough et al. reported that the short O−O distance can alter the four-proton reaction route and enhance the catalytic activity of $Na_{0.67}CoO_2$.[23] Meanwhile, oxygen stoichiometry always exists in an oxide semiconductor and plays an essential role in transport properties.[24] Wang et al. emphasized the crucial role of oxygen vacancies in the surface reconstruction for the OER of cobalt pnictides.[25] Oxygen vacancies should be taken into account in the electrochemical investigation of Na_xCoO_2. Qiao et al. claimed that Co in octahedra with low spin is energetically favorable for ORR.[20] Although the ORR activity of Na_xCoO_2 has rarely been reported, the characteristic of Co in CoO_6 octahedra with low spin states could make Na_xCoO_2 promising ORR catalysts for fuel cells.

The lattice dynamics, electronic structure, and coordination configuration of CoO_6 can be manipulated by altering Na concentration. This observation inspired us to explore the potential electrocatalytic activity of Na_xCoO_2 and try to unveil the effects of the Co valence states, the Co−O bond, and the electronic structure on its electrochemical OER and ORR performance. We found that the evolution of the electronic structure induced by Na extraction promotes Co−O bond strength, which is mainly responsible for the electrochemical activity of Na_xCoO_2, and it affects the reaction route related to the proton−electron transfer process. The appropriate lattice distortion and oxygen vacancies in the lattice dynamics are also recognized as advantages for electrochemical activity. This work provides new ways to manipulate the electronic and crystalline structures to improve the electrochemical activity of Na_xCoO_2 further.

■ EXPERIMENT AND METHODS

Materials and Synthesis. Na_xCoO_2 (x = 1.0, 0.9, 0.75, 0.5, and 0.3) samples were synthesized by a solid-state reaction method. All of the raw materials were used as received without further purification. Na_2CO_3 (Alfa Aesar, 99.95%) and Co_3O_4 (Alfa Aesar, 99.7%) were weighed according to each required stoichiometry ratio and then loaded into a stainless-steel vial (SPEX SamplePrep 8007) for mixing. For each sample, after high-energy ball-milling for 2 h, the powder was placed in a die with a 1/2 in. inner diameter and pressed into a pellet under 75 MPa pressure. The pellets were sintered at 900 °C in air for 12 h. The sintered pellets were ground into a powder for a second round of pressing and sintering with the abovementioned specifications. The final sintered pellets were ground and used as the catalysts. $Na_{0.75}CoO_\delta$ samples were obtained after annealing $Na_{0.75}CoO_2$ samples in a tube furnace under atmospheres with different O_2 concentrations determined by controlling the Ar/O_2 ratio.

Table 1. Physical and Electrochemical Properties of Na$_x$CoO$_2$, Including Lattice Constants, Na/Co Ratio Obtained from EDX, Calculated Weighted Redox Center, Electrical Resistivity Tested by the Standard Four-Probe Method, Deconvoluted O1/O2 Ratio in O1s XPS, Co^{4+}/Co^{3+} Quantified by XPS Deconvolution, Electrochemically Activated Surface Area (ECSA), and Activation Energy

	lattice parameters (Å)	Na/Co (Na$_x$CoO$_2$)	weighted redox center	electrical resistivity (Ohm m)	O1/O2 (XPS)	Co^{4+}/Co^{3+} (XPS) (%)	ECSA (cm^2)	activation energy (KJ mol^{-1})
NaCoO$_2$	a = 2.831662 c = 10.923512	0.97	1.3508	6.97×10^{-5}	0.7900	64	18.30	28
Na$_{0.75}$CoO$_2$	a = 2.829852 c = 10.934163	0.74	1.3500	7.06×10^{-5}	0.7750	79	10.83	18.8
Na$_{0.5}$CoO$_2$	a = 2.827000 c = 10.940804	0.58	1.3501	1.33×10^{-4}	0.7700	85	13.30	21.3
Na$_{0.3}$CoO$_2$	a = 2.821199 c = 11.013643	0.37		5.49×10^{-4}	0.7600	94	5	30

Rietveld Refinement. The powder X-ray diffraction spectra were collected on a PANalytical multipurpose diffractometer with an X'Celerator detector (PANalytical X'Pert Pro). The target powders were prepared by mixing the sintered Na$_x$CoO$_2$ (x = 1.0, 0.9, 0.75, 0.5, and 0.3) powder with standard reference Si by the mass ratio (1/1), which is used for calibration of diffraction line positions and line shapes. The data were collected from 10 to 135° with steps of 0.02°. The lattice parameters were refined using the FullProf Suite (2019 version) software package. The structure refinements were carried out according to space group $P6_322(182)$. Co, Na(1), Na(2), and O took the atomic positions 2a (0, 0, 0), 2b (0, 0, 1/4), 6h (2x, x, 1/4), and 4f (1/3, −1/3, z), respectively.

Electrochemical Measurement. The catalyst inks were prepared by mixing 5 mg of a Na$_x$CoO$_2$ (x = 1.0, 0.9, 0.75, 0.5, and 0.3) fine powder with 1 mg of acetylene black carbon, and then dispersing the mixture into a solution containing 0.75 mL of deionized (DI) water, 0.25 mL of ethanol, and 50 μL of a Nafion ionomer. The ink was horn-sonicated for 30 s, and then bath-sonicated for 30 min. A total of 15 μL of the catalyst ink was dropped onto a glassy carbon electrode (0.196 cm^{-2}), resulting in a loading mass of 382.6 μg cm^{-2}. The glassy carbon electrode was polished using a microcloth pad with a 0.05 μm α-Al$_2$O$_3$ slurry, and then ultrasonicated in ethanol and DI water until it was completely clean. Commercial Pt/C (20% on carbon black, Alfa Aesar) was directly used for catalyst ink preparation, and IrO$_2$ and Co$_3$O$_4$ catalysts were prepared using the production routine for catalyst inks described above. All electrochemical measurements in the study, including cyclic voltammetry (CV) and linear sweep voltammetry (LSV), were conducted using a Biologic SP-200 potentiostat with a standard three-electrode configuration in an alkaline electrolyte. All potentials were converted to the RHE scale by $E_{RHE} = E_{Hg/HgO} + 0.059$pH $+ 0.098$ and compensated with iR-corrected resistance of the electrolyte. A Pt plate and a Hg/HgO electrode were adopted as counter and reference electrodes, respectively. A thin film of each powder-based catalyst was placed on a glassy carbon electrode and the assembly was used as a working electrode. Each working electrode with a diameter of 5 mm was mounted in a rotation electrode (EDI 101, Lange) with a speed control unit (CTV101, HACH). LSV of current density was normalized to the geometric surface area. The polarization curves for OER were recorded by LSV with a scan rate of 5 mV s^{-1} and a rotating speed of 1600 rpm. CV scans were conducted over 200 cycles with a scan rate of 50 mV s^{-1} in the range of 1.225−1.575 (vs RHE) prior to measuring the polarization curves. This process was applied to all samples. Additionally, all of the electrocatalytic measurements were performed at room temperature (22 °C), except where otherwise specified.

ECSA (Electrochemical Active Surface Area). The electrochemical double-layer capacitance is obtained from $i_c = \nu C_{DL}$, where i_c is the double-layer charging or discharging current, ν is the scan rate, and C_{DL} is the double-layer capacitance. C_{DL} is extracted from the slope of the plot of i_c as a function of ν. ECSA is calculated from the double-layer capacitance according to the equation ECSA = $\frac{C_{DL}}{C_s}$,

where C_s is the specific capacitance of a sample per unit area in an identical electrolyte. In this work, C_s = 0.06 mF/cm^2.

Weighted Redox Center. The weighted redox center is defined as the average value of the weighted oxidation and reduction peak voltage on the RHE scale, which is determined by the formula $V_{weighted} = \int \frac{V \, dQ}{\int dQ}$, where Q is the charge corresponding to oxidation or reduction peaks at the voltage V.

Material Characterization. High-resolution X-ray photoelectron spectra were collected using a PHI Quantera XPS scanning microprobe with an Al monochromatic K$_\alpha$ source (15 KV, 20 mA). The chamber pressure was well controlled below 5×10^{-8} Torr. The surface morphology and composition characterizations were investigated using a scanning electron microscope (LEO 1525) and a transmission electron microscope with an energy-dispersive X-ray function (JEOL 2010F). The electrical conductivity was evaluated by a four-point probe method with a commercial equipment ULVAC ZEM3.

X-ray Absorption Spectroscopy (XAS) Measurements. X-ray absorption near-edge structure (XANES) experiments were performed at beamline 11-2 at the Stanford Synchrotron Radiation Lightsource of the SLAC National Accelerator Laboratory. A Co K-edge transmission signal was measured by the ionization chamber. All XAS data analyses were performed using Athena to extract XANES information.

Density Functional Theory (DFT) Calculation. The DFT calculations were conducted using the Vienna Ab initio Simulation Package (VASP). The projector augmented-wave (PAW) potentials were applied for electron−ion interactions. The generalized-gradient approximation (GGA) parametrized by Perdew−Burke−Ernzerhof (PBE) was used for the exchange−correlation functional. A cutoff energy of 450 eV was used for the plane-wave basis set. The k-space grid of $4 \times 4 \times 2$ was employed to sample the Brillouin zone of the 2 × 2 × 1 supercell of Na$_x$CoO$_2$. The electronic self-consistency calculation was assumed for a total energy convergence of less than 10^{-4} eV. All of the atomic positions were optimized until the interatomic forces were smaller than 0.03 eVÅ^{-1}.

RESULTS AND DISCUSSION

Rietveld Refinement and Morphology. Sodium cobaltite (Na$_x$CoO$_2$, x = 0.3, 0.5, 0.75, and 1.0) samples were synthesized by ball-milling and a solid-state reaction. X-ray diffraction (XRD) patterns were obtained to check the phase purity and crystallinity of the Na$_x$CoO$_2$ samples. As shown in Figure 1b, the main (002) peak confirms the typical layer structure along the c axis. NaCoO$_2$ exhibits phase purity with a hexagonal structure, and its small FWHM (full-width at half-maximum) defines its good crystallinity. It was found that Co$_3$O$_4$ begins to emerge as an impurity phase with Na deficiency and increases with decreasing Na concentration. The crystal structures of Na$_x$CoO$_2$ were refined, and their
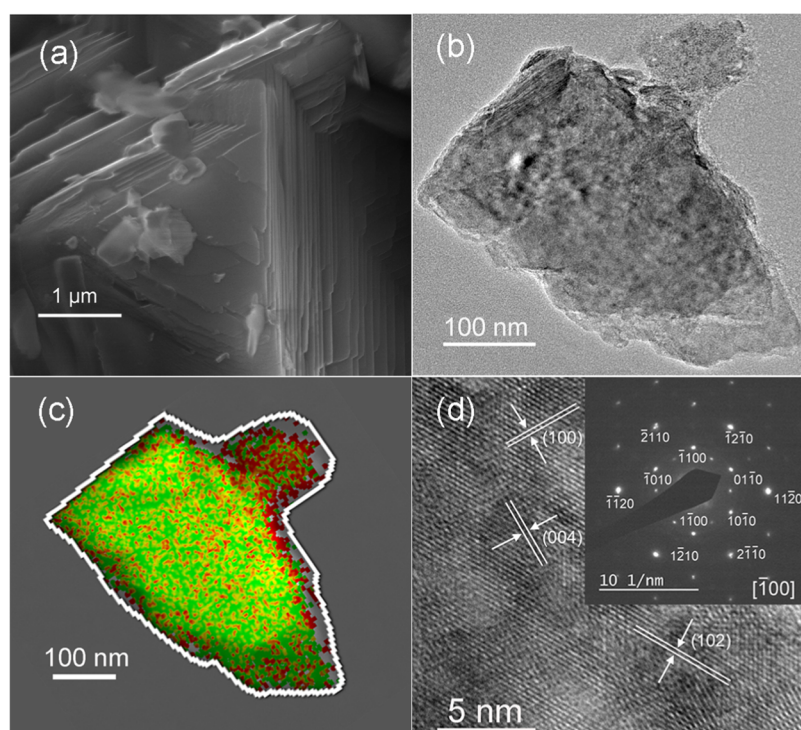
Figure 2. (a) SEM image of an as-prepared $Na_{0.75}CoO_2$ particle. (b, c) TEM image and corresponding EDX mapping of a post-OER $Na_{0.75}CoO_2$ particle. (d) High-resolution TEM image and (inset) its corresponding SAED pattern.

lattice parameters were determined by Rietveld refinement. The results are shown in Figures 1c and S1, in which the standard Si powder was used to correct the line position and the changes in the line width.[26] It was observed that the lattice parameter c increases from 10.9235 to 11.0136 Å as Na decreases from stoichiometric $x = 1.0$ to 0.3, which indicates that the layer separation along the crystallographic c axis is expanded [Figure 1d and Table 1]. Huang et al. observed that the thickness of the CoO_2 layers decreases when more Na is extracted from the ionic layer due to the reduced Coulombic attraction to the neighboring CoO_2 layer. The variation in layer separation offers a good opportunity to expose the activated sites.

The surface morphology of a freshly sintered Na_xCoO_2 powder is presented in Figure S2. Particles of all of the samples display a remarkably layered structure, and the single-layer size gradually increases with increasing Na concentration. The typical layer size can reach tens of micrometers in $Na_{0.75}CoO_2$ and $NaCoO_2$. The high-magnification image of an as-prepared $Na_{0.75}CoO_2$ particle in Figure 2a clearly shows that it is composed of multiple sheets stacked layer by layer. The surface morphology of the catalysts was also examined after OER measurement, as shown in Figure 2b, and it was found that particles 200−300 nm in size remained intact after 5000 cyclic voltammetry (CV) cycles and that the layered sheets can still be seen along their edge. Energy-dispersive X-ray spectroscopy (EDX) mapping results in Figures 2c and S3 show that Na and Co are evenly distributed throughout the nanoparticles after OER measurement. Somewhat surprisingly, a single-crystal characteristic was determined from selected-area electron diffraction (SAED) of a high-resolution TEM image obtained at the center of a $Na_{0.75}CoO_2$ particle after OER measurement. Figure 2d shows the existence of lattice fringes with spacings of 0.267, 0.241, and 0.217 nm, which correspond well with the

(004), (100), and (102) facets of $NaCoO_2$, respectively. Furthermore, the corresponding SAED pattern was indexed to the hexagonal phase along the $[\overline{1}00]$ zone axis [inset, Figure 2d]. The indexed diffraction pattern corresponds coherently to a hexagonal structure, and each spot is situated with strict order and repeatability. Additionally, a second hexagonal diffraction pattern was detected. As shown in Figure S4, the angular separation between the two patterns is 30° by rotation, which can be ascribed to crystal twisting induced by the lattice defects.

Tuning Co−O Covalency Bonding. The electronic density-of-states (DOS) of Na 3s, Co 3d, and O 2p for Na_xCoO_2 are displayed in Figure 3. Compared with the total DOS shown in Figure S5, Figure 3 illustrates that the contributions of the Co 3d (t_{2g}) and O 2p orbitals are essential to the electronic structure around the Fermi level. The Na 3s orbital has little correlation with O 2p, which suggests the ionic state of the Na between the CoO_2 sheets that energetically enables Na-ion charge and discharge in a sodium-ion battery.[27] As shown in Figure 3a, the conduction band in $NaCoO_2$ originates from the hybridization of two Co 3d(e_g) orbitals with O 2p, leading to the large splitting of the bonding and antibonding orbitals. In most metal oxides, the Co $3d$ orbitals are more energetic than the O 2p orbitals. However, in $NaCoO_2$, Co 3d and O 2p exhibit strongly hybridized behavior, suggesting the high spatial overlap and energetic similarity of the electronic states of Co and O. The valence band is primarily determined by the overlapping of the other three Co 3d(t_{2g}) and O 2p orbitals. It can be seen that the Fermi level of $NaCoO_2$ is pinned in the valence band. It gradually submerges deeply into the valence band with increasing Na extraction, as shown in Figure S5,[14,17] which produces more charge carriers in the valence band that contribute to the charge transfer. A schematic illustration of
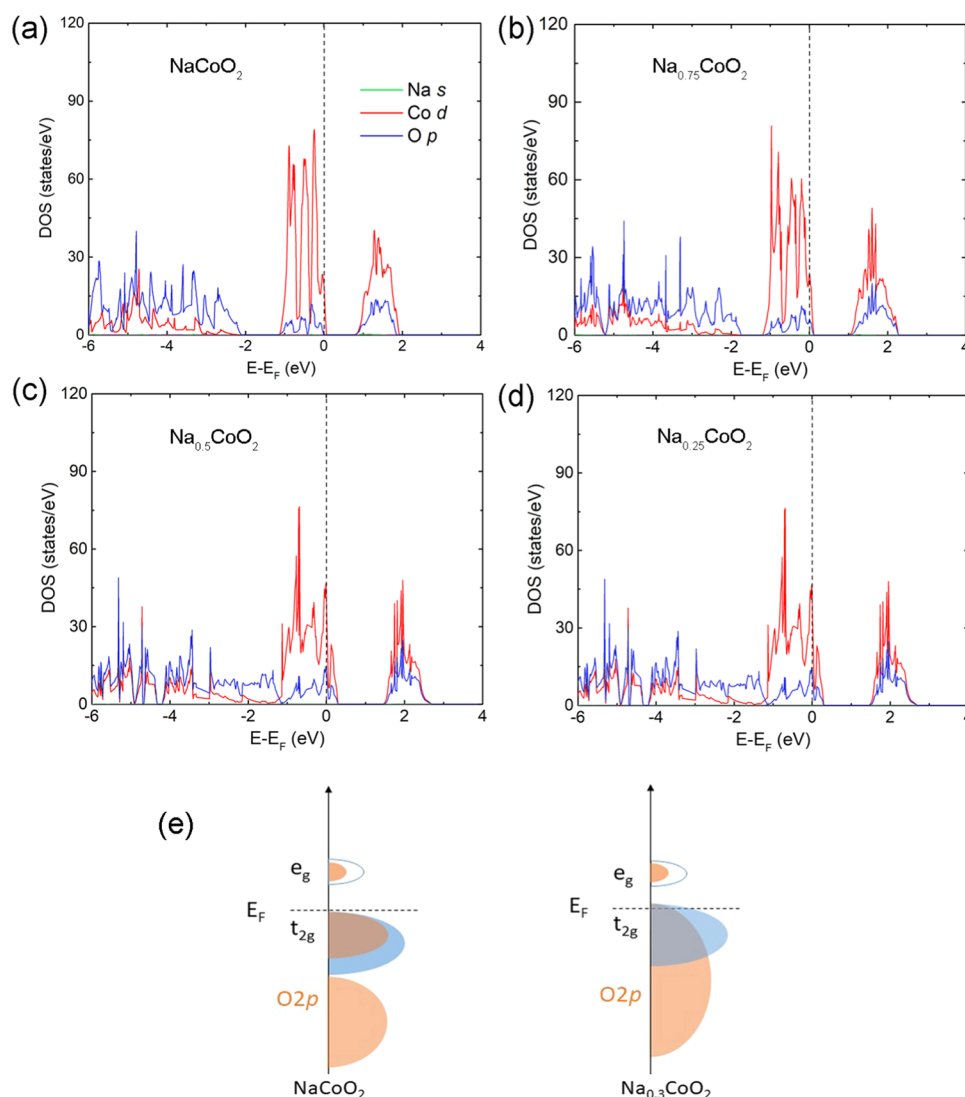
Figure 3. Electronic density-of-states of Na s, Co d, and O p for Na_xCoO_2 calculated by DFT. (a) $NaCoO_2$, (b) $Na_{0.75}CoO_2$, (c) $Na_{0.5}CoO_2$, and (d) $Na_{0.25}CoO_2$. (e) Schematic illustration of the band diagram change with different Na concentrations.

the band diagram change is shown in Figure 3e. More holes are created when the Fermi level descends deeper into the O 2p orbital with increasing Na extraction, as shown in Figure 3, leading to the O_2/H_2O redox potential approaching the O 2p states of the oxides. Subsequently, the lattice oxygen participation in the OER becomes thermodynamically favorable.[28] With increasing Na extraction from the lattice, it can also be seen that O 2p states located below −2 eV increase to mix with Co 3d, leading to enhanced covalency bonding between Co and O atoms. The transition metal−oxygen bond covalency is a reliable parameter to rationalize the OER activity. The enhanced covalency has been suggested to thermodynamically lower the energy barrier for OER and facilitate the charge transfer between the transition metal and the oxygen.[29] Both the metallic feature and the strong covalent bonding between Co and O observed in Na_xCoO_2 allow it to be a good OER catalyst.

X-ray Photoelectron Spectroscopy (XPS) and Fourier Transform Infrared Spectroscopy (FTIR). X-ray absorption near-edge structure (XANES) analysis was conducted to elucidate the oxidation states variation of Co in Na_xCoO_2 due to the high sensitivity of the technique to the oxidation

states of the transition metals. The XANES spectra of Co^{3+} in $LiCoO_2$ and $Co^{3.6+}$ in $Sr_6Co_5O_{15}$ were collected as the reference states, as shown in Figure 4a. The first derivative of the XANES spectra of the Co K-edge is shown in Figure 4b. It can be observed that $Na_{0.75}CoO_2$ indeed has a higher average covalence state than $NaCoO_2$, indicating increased Co^{4+} concentration with Na extraction and that both samples have oxidation states that are higher than Co^{3+} and lower than $Co^{3.6+}$. The separated peaks in Na_xCoO_2 might suggest the coexistence of Co^{3+} and Co^{4+}. XPS of Na_xCoO_2 was collected to examine its surface chemical states. All of the spectra were corrected by the relative position of the C1s before conducting any further deconvolution. The deconvolutions of Co 2p XPS were carefully performed based on the XANES analysis and the relative change of Co^{4+}/Co^{3+} was determined to rationalize the evolution of weighted redox peaks in Na_xCoO_2. As shown in Figure 4c, the two prominent peaks are identified as Co $2p_{3/2}$ and Co $2p_{1/2}$ and result from the orbit-spinning splitting with separation around $\Delta = 15$ eV.[30,31] The main Co $2p_{3/2}$ peak is deconvoluted into two central peaks, which are assigned to Co^{3+} and Co^{4+}.[10,32] Two satellites attributed to the Co d wave functions are related to the charge transfer between Co and
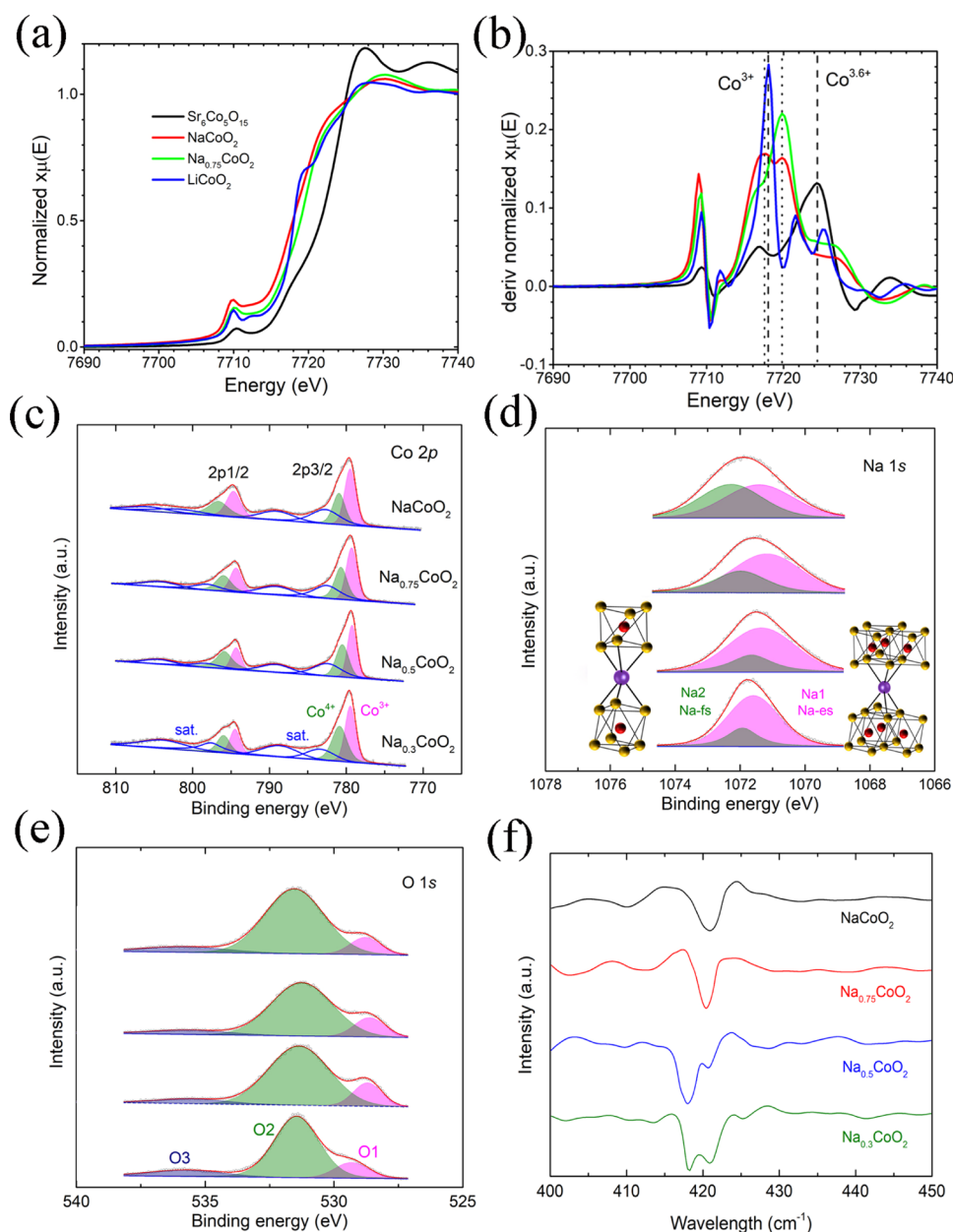
Figure 4. (a) XANES spectra of the Co K-edge in $NaCoO_2$ and $Na_{0.75}CoO_2$ with $LiCoO_2$ (Co^{3+}) and $Sr_6Co_5O_{15}$ ($Co^{3.6+}$) as references, and (b) corresponding first derivative of the XANES. XPS deconvolution of (c) Co 2p, (d) Na 1s, and (e) O 1s of Na_xCoO_2 (x = 1, 0.75, 0.5, and 0.3, top to bottom). Left and right insets in (d): diagrams showing face-shared (Na-fs) and edge-shared (Na-es) Na ions (purple spheres), respectively, in Na_xCoO_2. (f) FTIR of Na_xCoO_2.

O.[4,33] There is no noticeable peak shift of Co^{3+} or Co^{4+} between the Na_xCoO_2 samples. It is of particular interest that the relative ratio of Co^{4+}/Co^{3+}, which is quantified from the deconvoluted peak area, increases with decreasing Na concentration (Table 1), which follows from the increased average valence states of Co with less Na in the lattice.[18]

As shown in Figure 4d, the deconvolutions of Na 1s in Na_xCoO_2 are fitted with two peaks located around 1071.3 and 1072.4 eV and interpreted as the two sites of Na1 and Na2, respectively, in the Na ionic layer. Na1 and Na2 correspond to the Na ions with edge- and face-sharing coordination, respectively, as shown in the respective right and left inset diagrams in Figure 4d.[27] The Na ions edge-shared with the CoO_6 octahedra exist over the entire range of Na variation. With decreasing Na content, the deconvoluted peak

corresponding to the face-sharing coordination becomes weaker, indicating possible structural evolution due to the changed coordination, which might result in the lattice distortion of the CoO_6 octahedra.

The XPS spectra of O 1s are deconvoluted into three peaks labeled as O1, O2, and O3 in Figure 4e. The O1 peak is typically associated with an oxygen−metal bond, indicating oxygen in the lattice. The O2 peak is assigned to adsorption oxygen species and the low-coordinated oxygen ions. The O3 peak is commonly recognized as resulting from the carbon−oxygen species. The formation of the O2 peak is interpreted as indicating the presence of an oxygen-deficient environment and is closely related to the oxygen defects. The quantified O1/O2 ratio in Na_xCoO_2 is provided in Table 1, and it is found that a significant number of oxygen defects are
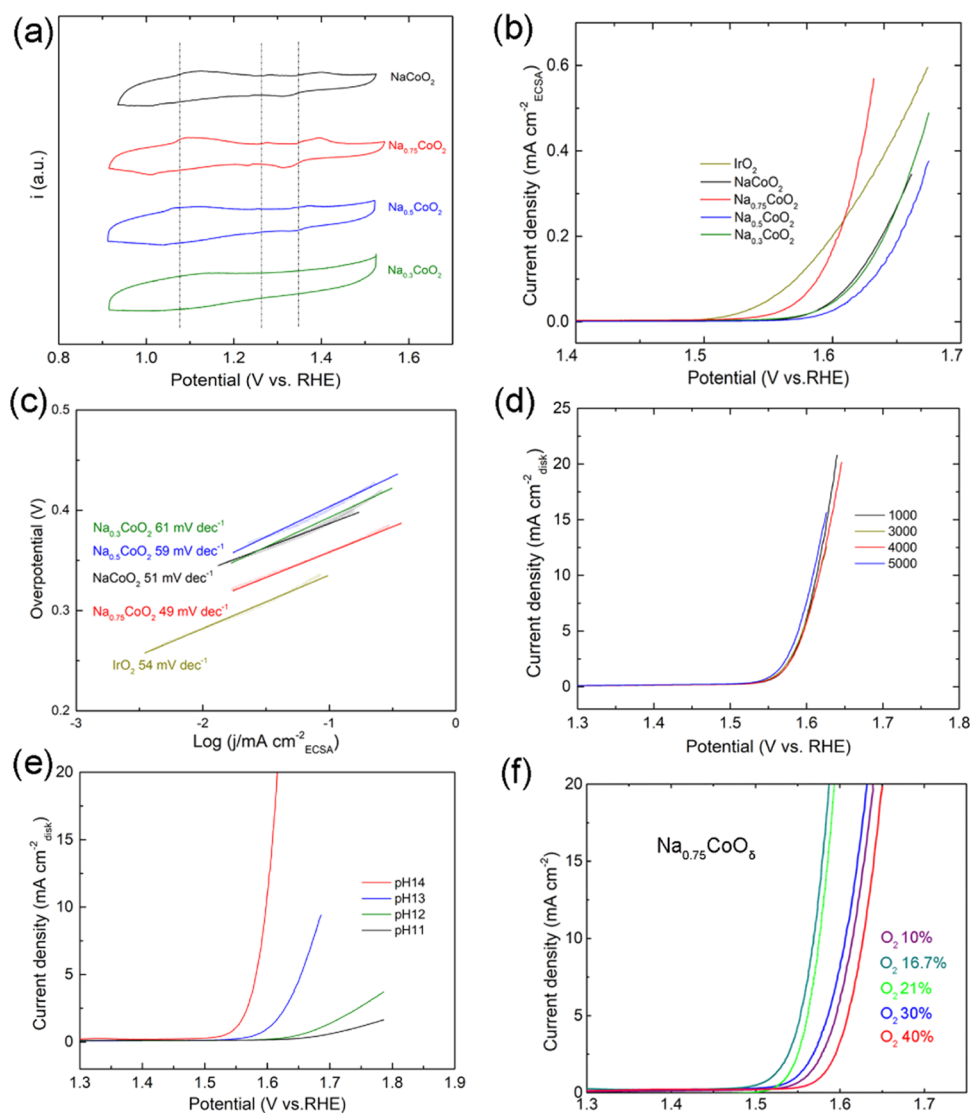
Figure 5. (a) CV of Na_xCoO_2 with three sets of redox peaks indicated by dashed lines. (b) LSV curves for OER of Na_xCoO_2 and IrO_2 in 1 M NaOH with current density normalized to ECSA. (c) Tafel slopes extracted from the LSV curves in (b). (d) LSV curves recorded after every 1000 CV cycles to evaluate OER stability of $Na_{0.75}CoO_2$. (e) pH-dependent LSV curves for OER of $Na_{0.75}CoO_2$. (f) LSV of $Na_{0.75}CoO_\delta$ after annealing in atmospheres with different O_2 concentrations.

predicated on increased Na deficiency. Oxygen vacancies exist in most cobalt-oxide-based catalysts. It has been reported that oxygen vacancies can promote surface reconstruction, increase the activated sites, and speed up interface charge transfer during OER activity.[34−36] Therefore, the oxygen vacancies in the Na_xCoO_2 lattice could positively affect its OER performance.

Co^{3+} with octahedral coordination is considered stable in the spinel oxides. With Na extracted from the lattice, the Co valence states inevitably increase to compensate for the charge balance, resulting in expected lattice distortion of the octahedra. Fourier transform infrared spectroscopy (FTIR) can provide precise information regarding the deformation and vibration of the Co−O bond. FTIR of Na_xCoO_2 was performed at room temperature, and the results are shown in Figures 4f and S6. The observed bands are distinctly correlated with the stretching vibration of Co−O and the bending mode of O−Co−O in the CoO_6 octahedra. The absorption bands at 421 cm^{-1} [Figure 4f] are closely associated with O−Co−O deformation modes in the CoO_6 octahedra. The characteristic

bands at 655 cm^{-1} (Figure S6) are assigned to the Co−O stretching vibration.[29,37,38] With decreasing Na concentration, the bands at 421 and 655 cm^{-1} show apparent changes in shape and line position, which are directly related to changes in the bonding distance and angle of O−Co−O in the CoO_2 sheets. The absorption bands at 421 cm^{-1} are noticeably split into two as Na is extracted, which is ascribed to increased O−Co−O vibration energy due to the intrinsic lattice distortion in the CoO_2 layer, as well as the increased Co^{4+} branch in the CoO_6 octahedra. The slight blue shift in the frequency matches the decreased Co−O bond distance,[13] which is induced by the charge transfer accompanying the decreased Na concentration. FTIR thus provides direct evidence that, with decreasing Na concentration, changes in the sites occupied by Na1 and Na2 lead to lattice distortion in the CoO_2 layers.

Electrochemical Properties. The electrochemical OER activity of Na_xCoO_2 was evaluated in a 1 M NaOH electrolyte using a standard three-electrode configuration. The CV of Na_xCoO_2 is displayed in Figure 5a, in which three sets of reversible redox peaks located at around 1.08, 1.25, and

$1.35V_{RHE}$ are indicated by dashed lines. It has been suggested that the redox peaks of 1.08 and $1.35V_{RHE}$ are nominally assigned to hydroxide-mediated protonation/deprotonation associated with Co^{2+}/Co^{3+} and Co^{3+}/Co^{4+} redox processes, respectively.[28,39,40] The reason for the appearance of the $1.25V_{RHE}$ redox peak here remains unclear. Meanwhile, it is noticeable that the redox peak located at around $1.35V_{RHE}$ disappears when the Na content approaches 0.3. The redox peaks are straightforwardly related to the valence states of Co and its electronic structure, while XPS deconvolution and XANES analysis show that increasing Na extraction leads to an increased intensity of the Co^{4+}/Co^{3+} spectra ratio and a higher average oxidation state of Co, respectively. The relatively increased Co^{4+} in $Na_{0.3}CoO_2$ might thus deactivate the redox peak at $1.35V_{RHE}$.

The redox peaks in the reversible oxidation/reduction process of transition metals (Ni, NiFe, and Co) typically occur before the onset of OER.[41,42] A positive shift in the position of the redox peaks accompanies improved OER activity in most cases.[43] Shao-Horn et al. also suggested that such a positive shift reflects the redistribution of charge between a substituting metal and a parent metal, promoting the Gibbs free energy of adsorption and desorption toward intermediate energy during the protonation/deprotonation process, which is beneficial for improving OER performance.[44] The phenomenon in which varied covalency states of Co are induced by different Na concentrations prompts the question whether Na directly affects the OER activity of Na_xCoO_2.

The calculated weighted redox peak centers for Na_xCoO_2 are shown in Table 1. No apparent shift is observed with changes in Na concentration. Karppinen et al. suggested that the charge imbalance in the CoO_2 layer would be compensated by the oxygen vacancies once the average valence state of Co (Co^{3+} and Co^{4+}) increases to a particular value.[45] Although both Na and vacancies directly modulate the average valence state of Co, neither directly affects the electrochemical redox reaction. The possibility of charge transfer between Co^{3+}, Co^{4+}, and even Co^{2+} during their protonation/deprotonation processes is also excluded, consistent with the XPS results. Increased Co^{4+} concentration might be inert in regard to increased OER kinetics.
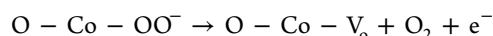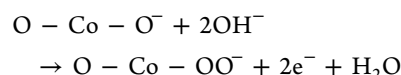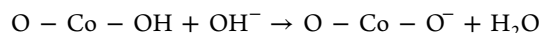
Co with CoO_6 octahedra coordination is critical to superior OER performance in many Co-based spinel-structure oxides and perovskites.[46] Density functional theory (DFT) calculations and FTIR suggest that Na variation influences the electronic and coordination environment of CoO_6 octahedra. It has been demonstrated that the holes transfer along the O−Co−O chain in the CoO_2 layer, where the vacancies and the lattice distortion also play critical roles. It could be speculated that Na variation does not affect the electrochemical properties directly but rather the electronic structure of Co in general and that the oxygen vacancies and lattice distortion also reasonably contribute to OER activity, which will be discussed in more detail below.

Linear sweep voltammetry (LSV) was recorded in an O_2-saturated electrolyte, and the curves are shown in Figure 5b. The current densities of Na_xCoO_2 and IrO_2 were normalized to their ECSA values. The catalytic activity of Na_xCoO_2 was found to be Na-dependent and the performance generally becomes worse with reduced Na concentration, although $Na_{0.75}CoO_2$ displays the best OER performance among the Na_xCoO_2 samples. Comparatively, IrO_2 exhibits the lowest onset po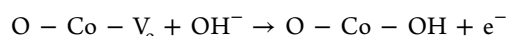tential, but its activity becomes sluggish at high current density. The current densities of Na_xCoO_2, IrO_2, and Co_3O_4 were also normalized to their geometric surface areas, as shown in Figure S7a. The OER activity of Co_3O_4 is shown since this exists as an impurity phase in the highly Na-deficient samples. Owing to its poor activity and minimal content in the samples, the influence of Co_3O_4 on the OER performance of Na_xCoO_2 is negligible. The best catalytic activity among the Na_xCoO_2 samples was found in $Na_{0.75}CoO_2$, which exhibits a current density of 10 mA cm^{-2} at an overpotential of 370 mV, comparable to the performance of IrO_2. The highest kinetics of $Na_{0.75}CoO_2$ was also confirmed by the Tafel slopes displayed in Figure 5c, which shows that $Na_{0.75}CoO_2$ exhibits the lowest Tafel slope of 49 mV dec^{-1}. To further rationalize the OER activity of Na_xCoO_2, the charge-transfer resistance and the electrochemical active surface area (ECSA) of each of the samples are shown in Figure S7b and Table 1, respectively. Although all of the Na_xCoO_2 samples exhibit high charge-transfer resistance at the interface, much higher than that of NiFe (oxy)hydroxide,[47,48] $Na_{0.75}CoO_2$ displays the lowest charge-transfer resistance among the samples studied, as indicated by the electrochemical impedance spectroscopy curves shown in Figure S7b, which contributes to its low onset potential and competent performance. $Na_{0.75}CoO_2$ also has high bulk electrical conductivity benefiting from its good crystallinity and optimized Na concentration. Reducing the charge-transfer resistance of $Na_{0.75}CoO_2$ at the interface would thus provide an excellent opportunity to improve its catalytic activity further. The Na-dependent ECSA of Na_xCoO_2 is presented in Table 1, and the corresponding double-layer capacitance values of Na_xCoO_2 and IrO_2 are shown in Figure S7c. Rietveld refinement shows that Na extraction leads to lattice expansion along the c axis [Figure 1d and Table 1], which is mainly contributed by the increased Na_2O layer.[13] Additionally, the CoO_2 layer is compressed due to reduced Coulombic attraction between neighboring CoO_2 layers once the filling degree of Na is decreased. The ECSA of Na_xCoO_2 exhibits a consistent dependence on the variable thickness of the CoO_2 layer.[13] The high OER activity of $Na_{0.75}CoO_2$ benefits from its low interface charge-transfer resistance and the large exposed surface area. The OER activity of $Na_{0.75}CoO_2$ is also highly stable, and its LSV curve maintains its original potential and shape after 5000 cycles [Figure 5d], which should be ascribed to the catalyst's layered structure and good crystallinity.

pH Dependence and Mechanism of OER. The DFT calculations in Figure 3 show that $Na_{0.75}CoO_2$ has improved Co−O covalency and specific electronic states with a strong O 2p characteristic near the Fermi level, which could make the lattice oxygen active in the OER process.[28] To reveal the reaction mechanism of OER in $Na_{0.75}CoO_2$, the pH dependence of its OER activity was also studied. Figure 5e shows that the OER performance of $Na_{0.75}CoO_2$ on the RHE scale increases with increasing pH value of the electrolyte. This same phenomenon was observed in other Co-based perovskites $SrCoO_3$ and $Pr_{0.5}Ba_{0.5}CoO_3$, indicating that the lattice oxygen atoms are activated.[28,35] The lattice oxygen shows comparable kinetics with Co sites when the Fermi level descends deeper into the O 2p orbitals. In contrast to the conventional OER mechanism that involves proton−electron transfer steps (hydroxide deprotonation, peroxide formation, peroxide deprotonation, and hydroxide regeneration) in concert at the surface metal site, the OER reaction with lattice oxygen participation is suggested to involve a decoupled proton−

electron transfer process. There are several possible mechanisms of pH dependence related to different rate-determining steps, and the explanations are also material-dependent. For $Na_{0.75}CoO_2$ with strong metal−oxygen covalency, the rate-determining step is proposed to be the deprotonation of surface hydroxyl at the lattice oxygen site. The reaction route is described as

$$O - Co - OH + OH^- \rightarrow O - Co - O^- + H_2O$$

$$O - Co - O^- + 2OH^-$$
$$\rightarrow O - Co - OO^- + 2e^- + H_2O$$

$$O - Co - OO^- \rightarrow O - Co - V_o + O_2 + e^-$$

and

$$O - Co - V_o + OH^- \rightarrow O - Co - OH + e^-$$

This reaction route shows that the lattice oxygen actively participates in the OER reaction. The oxygen vacancies and oxygen motion in the lattice play an essential role during the protonation/deprotonation process. To validate the effects of lattice oxygen on OER, $Na_{0.75}CoO_\delta$ samples were obtained by annealing $Na_{0.75}CoO_2$ in atmospheres with different O_2 concentrations. It has been demonstrated that oxygen vacancies and lattice oxygen in metal oxides are controllable when annealing in different oxygen concentrations.[49] As shown in Figure S8, the strong oxygen-concentration dependence of the electrical conductivity confirms that oxygen concentration in the lattice can be manipulated by controlling the annealing atmosphere, and further that the electrical structure is also directly affected. The OER performance of $Na_{0.75}CoO_\delta$ also displays a strong dependence on the variation of the O_2 concentration, as shown in Figure 5f. It is thus evident that oxygen vacancies or lattice oxygen can directly affect OER performance. Although the oxygen vacancies have been demonstrated to be important for the surface reconstruction or charge transfer for the OER and synergistic effects from Na nonstoichiometry and oxygen vacancies are also expected, more efforts are needed to clarify their effects in the oxides with strong metal−oxygen covalency.

Activation Energy. It has been previously demonstrated that the energy barrier for OER could be reduced when the O 2p position in the Fermi level approaches the O_2/H_2O redox energy. The activation energy can be fundamentally helpful in confirming this. The Na_xCoO_2 energetics were investigated by exploring the temperature dependence of their catalytic activity.[50,51] LSV curves were recorded from 25 to 45 °C and are displayed in Figure S9, which shows that OER activity exhibits noticeable improvement with elevated temperature, indicating that the activation energy is thermodynamically temperature-sensitive. The activation energy (E_a) for OER is calculated by the Arrhenius relationship, $\frac{d\log(j_0)}{d\frac{1}{T}} = -\frac{E_a}{2.3R}$, where j_0, T, and R are the exchange current density, ambient temperature, and the universal gas constant, respectively, as shown in the insets of Figure S9. The composition-dependent activation energy of Na_xCoO_2 is shown in Figure 6a and provided in Table 1, and it exhibits an inverse dome shape with the lowest activation energy of 18.8 KJ mol^{-1} observed in $Na_{0.75}CoO_2$, nearly approaching that reported for IrO_2.[52] Such a low activation energy verifies that $Na_{0.75}CoO_2$ is highly energetic, making it a good OER catalyst.
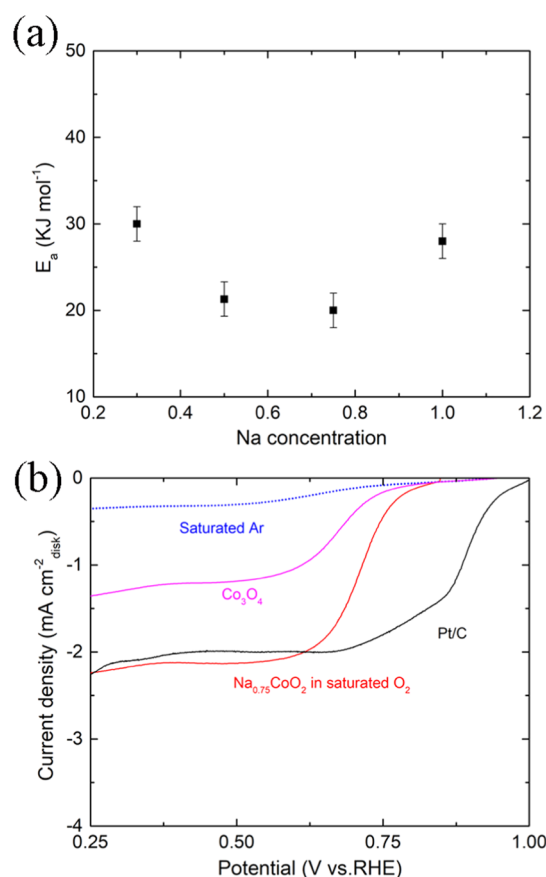

Figure 6. (a) Activation energy of Na_xCoO_2 as a function of the Na concentration. (b) Comparison of ORR activity between $Na_{0.75}CoO_2$ in O_2- and Ar-saturated electrolytes, Co_3O_4, and Pt/C.

Oxygen Reduction Reaction. Many Co-based spinel oxides display adequate ORR activity for potential application in fuel cells and metal−air batteries. The features of Co in Na_xCoO_2, including its strong Co−O covalency and low spin states in octahedral coordination, inspired us to explore the ORR activity of these catalysts, particularly since this has rarely been reported previously. The ORR catalytic activity of Na_xCoO_2 was experimentally determined in an O_2-saturated electrolyte. As shown in Figure S10a, Na_xCoO_2 exhibits significantly improved ORR activity compared with that of Co_3O_4, and $Na_{0.75}CoO_2$ displays the best ORR performance among the Na_xCoO_2 samples. As shown in Figure 6b, intrinsic $Na_{0.75}CoO_2$ exhibits no activity in an Ar-saturated electrolyte. In contrast, its apparent ORR activity accompanying an increased diffusion limit of its current density is observed in the O_2-saturated electrolyte. $Na_{0.75}CoO_2$ exhibits a half-wave potential of $0.74 V_{RHE}$, making it competitive with other Co-based catalysts for ORR.[20] Additionally, this ORR process shows high selectivity of O_2 to H_2O with an electron transfer number of 3.86 as rationalized by Koutecký-Levich plots extracted from the rotation-speed-dependent ORR activity of $Na_{0.75}CoO_2$ at different potentials [Figure S10b,c]. It should be noted that the ORR activity of $Na_{0.75}CoO_2$ still falls far behind that of the state-of-the-art Pt-based catalysts [Figure 6b], which presents a considerable challenge to improve its activity further. Such improvement in the catalytic activity of $Na_{0.75}CoO_2$ for ORR can be anticipated by modulating its spin states or employing bimetal substitution to optimize its Co−O covalency.

CONCLUSIONS

Bulk polycrystalline Na_xCoO_2 samples with different structures corresponding to varied Na concentrations were successfully synthesized. The evolution of the crystal structure and hybridization of the Co 3d and O 2p orbitals induced by changing the Na concentration is well understood. It was revealed that increased Co^{4+} concentration or a higher average oxidation state of Co is inconsequential to the OER activity of Na_xCoO_2, but the Co−O bond and the electronic structure of O 2p near the Fermi level, as well as the lattice distortion in the CoO_6 octahedra detected by TEM and FTIR, were found to contribute to such activity. Although DFT calculations and the dependence of OER activity on both pH and oxygen concentration strongly suggest that lattice oxygen is also critical to the OER reaction mechanism and catalytic sites in Na_xCoO_2, more efforts are needed to clarify the proton−electron transfer process. $Na_{0.75}CoO_2$ in particular displays superior OER activity compared to noble-metal-based catalysts, which is ascribed to its strong Co−O covalent bonding, larger electrochemical surface area, low charge-transfer resistance, and low activation energy. Additionally, the structure and electrochemical merits of Na_xCoO_2 provide a solid foundation upon which its ORR activity can be further improved to reach the state-of-the-art.

ASSOCIATED CONTENT

Ⓢ Supporting Information

The Supporting Information is available free of charge at https://pubs.acs.org/doi/10.1021/acs.chemmater.1c00008.

Rietveld refinement of Na_xCoO_2; SEM images of Na_xCoO_2; EDX mapping of $Na_{0.75}CoO_2$; SEAD of $Na_{0.75}CoO_2$ after OER measurement; DOS of Na_xCoO_2; FTIR of Na_xCoO_2; electrochemical properties (LSV, EIS, and double-layer capacitance) of Na_xCoO_2, IrO_2, and Co_3O_4; electrical conductivity of $Na_{0.75}CoO_\delta$; LSV of Na_xCoO_2 over the temperature range from 25 to 45 °C; ORR activities of Na_xCoO_2 and Co_3O_4; and Koutecký-Levich plots (PDF)

AUTHOR INFORMATION

Corresponding Authors

Qinyong Zhang − *Key Laboratory of Fluid and Power Machinery of Ministry of Education, School of Materials Science and Engineering, Xihua University, Chengdu 610039, China*; Email: bohr123@163.com

Shuo Chen − *Department of Physics and Texas Center for Superconductivity at University of Houston (TcSUH), Houston, Texas 77204, United States*; Email: schen34@uh.edu

Zhifeng Ren − *Department of Physics and Texas Center for Superconductivity at University of Houston (TcSUH), Houston, Texas 77204, United States;* ⓞ orcid.org/0000-0001-8233-3332; Email: zren@uh.edu

Authors

Shaowei Song − *Department of Physics and Texas Center for Superconductivity at University of Houston (TcSUH), Houston, Texas 77204, United States*

Yaqin Wang − *Key Laboratory of Fluid and Power Machinery of Ministry of Education, School of Materials Science and Engineering, Xihua University, Chengdu 610039, China*

Ryan C. Davis − *SLAC National Accelerator Laboratory, Menlo Park, California 94025, United States*

Zhensong Ren − *Department of Physics and Texas Center for Superconductivity at University of Houston (TcSUH), Houston, Texas 77204, United States*

Xin Xiao − *Department of Physics and Texas Center for Superconductivity at University of Houston (TcSUH), Houston, Texas 77204, United States*

Guang Yang − *Materials Science and Engineering Program and Texas Center for Superconductivity at University of Houston (TcSUH), University of Houston, Houston, Texas 77204, United States*

Dezhi Wang − *Department of Physics and Texas Center for Superconductivity at University of Houston (TcSUH), Houston, Texas 77204, United States*

Jiming Bao − *Materials Science and Engineering Program and Texas Center for Superconductivity at University of Houston (TcSUH), University of Houston, Houston, Texas 77204, United States*

Complete contact information is available at:
https://pubs.acs.org/10.1021/acs.chemmater.1c00008

Author Contributions

Z.R. supervised S.S. on designing the experiments; S.S. performed the material synthesis and measurements; S.S., Y.W., and Q.Z. performed the DFT calculations; S.S., Z.R., X.X., and S.C. carried out the data analysis; D.W. and S.S. conducted the TEM and SEM characterizations; S.S. performed X-ray photoelectron spectroscopy; S.S., G.Y., and J.B. carried out FTIR and data analysis; and R.C.D. conducted XAS measurements. Everyone contributed to writing the paper.

Notes

The authors declare no competing financial interest.

REFERENCES

(1) Hong, W. T.; Stoerzinger, K. A.; Lee, Y.-L.; Giordano, L.; Grimaud, A.; Johnson, A. M.; Hwang, J.; Crumlin, E. J.; Yang, W.; Shao-Horn, Y. Charge-transfer-energy-dependent oxygen evolution reaction mechanisms for perovskite oxides. *Energy Environ. Sci.* **2017**, *10*, 2190.

(2) Zhang, B.; Zheng, X.; Voznyy, O.; Comin, R.; Bajdich, M.; García-Melchor, M.; Han, L.; Xu, J.; Liu, M.; Zheng, L.; García de Arquer, F. P.; Dinh, C. T.; Fan, F.; Yuan, M.; Yassitepe, E.; Chen, N.; Regier, T.; Liu, P.; Li, Y.; De Luna, P.; Janmohamed, A.; Xin, H. L.; Yang, H.; Vojvodic, A.; Sargent, E. H. Homogeneously dispersed multimetal oxygen-evolving catalysts. *Science* **2016**, *352*, 333.

(3) Yu, F.; Yu, L.; Mishra, I. K.; Yu, Y.; Ren, Z. F.; Zhou, H. Q. Recent developments in earth-abundant and non-noble electrocatalysts for water electrolysis. *Mater. Today Phys.* **2018**, *7*, 121.

(4) Ohtaki, M. Thermoelectric Properties and Crystal Chemistry of Promising Oxide Candidate Na_xCoO_2, *ICT, Proc.*, 1999; p. 565.

(5) Ong, N. P.; Cava, R. J. Electronic frustration on a triangular lattice. *Science* **2004**, *305*, 52.

(6) Berthelot, R.; Carlier, D.; Delmas, C. Electrochemical investigation of the P2−Na$_x$CoO$_2$ phase diagram. *Nat. Mater.* **2011**, *10*, 74.

(7) Kubota, K.; Asari, T.; Yoshida, H.; Yaabuuchi, N.; Shiiba, H.; Nakayama, M.; Komaba, S. Understanding the structural evolution and redox mechanism of a NaFeO$_2$−NaCoO$_2$ solid solution for sodium-ion batteries. *Adv. Funct. Mater.* **2016**, *26*, 6047−6059.

(8) Jansen, M.; Hoppe, R. Notiz zur Kenntnis der Oxocobaltate des Natriums. *Z. Anorg. Allg. Chem.* **1974**, *408*, 104.

(9) Fouassier, C.; Matejka, G.; Reau, J. M.; Hagenmuller, P. Sur de nouveaux bronzes oxygenes de formule Na$_x$CoO$_2$ (x≤1). *J. Solid State Chem* **1973**, *6*, 532.

(10) Koshibae, W.; Tsutsui, K.; Maekawa, S. Thermopower in cobalt oxides. *Phys. Rev. B* **2000**, *62*, 6869.

(11) Fujita, K.; Mochida, T.; Nakamura, K. High-temperature thermoelectric properties of Na$_x$CoO$_{2-\delta}$ single crystals. *Jpn. J. Appl. Phys.* **2001**, *40*, 4644.

(12) Delmas, C.; Fouassier, C.; Hagenmuller, P. Structural classification and properties of the layered oxides. *Phys. B+C* **1980**, *99*, 81.

(13) Huang, Q.; Foo, M. L.; Pascal, R. A.; Lynn, J. W.; Toby, B. H.; He, T.; Zandbergen, H. W.; Cava, R. J. Coupling between electronic and structural degrees of freedom in the triangular lattice conductor Na$_x$CoO$_2$. *Phys. Rev. B* **2004**, *70*, No. 184110.

(14) Terasaki, I. Physics of the Thermoelectric Oxide NaCo$_2$O$_4$: A Guide to New Thermoelectric Oxides, *ICT Proc.*, 2002; p. 185.

(15) Terasaki, I. High-temperature oxide thermoelectrics. *J. Appl. Phys.* **2011**, *110*, No. 053705.

(16) Terasaki, I.; Sasago, Y.; Uchinokura, K. Large thermoelectric power in NaCo$_2$O$_4$ single crystals. *Phys. Rev. B* **1997**, *56*, No. R12685.

(17) Foo, M. L.; Wang, Y.; Watauchi, S.; Zandbergen, H. W.; He, T.; Cava, R. J.; Ong, N. P. Infrared probe of the electronic structure and charge dynamics of Na$_{0.7}$CoO$_2$. *Phys. Rev. Lett.* **2004**, *92*, No. 247001.

(18) Lin, H. J.; Chin, Y. Y.; Hu, Z.; Shu, G. J.; Chou, F. C.; Ohta, H.; Yoshimura, K.; Hébert, S.; Maignan, A.; Tanaka, A.; Tjeng, L. H.; Chen, C. T. Local orbital occupation and energy levels of Co in Na$_x$CoO$_2$: A soft x-ray absorption study. *Phys. Rev. B* **2010**, *81*, No. 115138.

(19) Kirsanova, M. A.; Okatenko, V. D.; Aksyonov, D. A.; Forslund, R. P.; Mefford, J. T.; Stevenson, K. J.; Abakumov; Artem, M. Bifunctional OER/ORR catalytic activity in the tetrahedral YBaCo$_4$O$_{7.3}$ oxide. *J. Mater. Chem. A* **2019**, *7*, 330.

(20) Mu, C.; Mao, J.; Guo, J.; Guo, Q.; Li, Z.; Qin, W.; Hu, Z.; Davey, K.; Ling, T.; Qiao, S.-Z. Rational design of spinel cobalt vanadate oxide Co$_2$VO$_4$ for superior electrocatalysis. *Adv. Mater.* **2020**, *32*, No. 1907168.

(21) Grimaud, A.; Carlton, C. E.; Risch, M.; Hong, W. T.; May, K. J.; Shao-Horn, Y. Oxygen evolution activity and stability of Ba$_6$Mn$_5$O$_{16}$, Sr$_4$Mn$_2$CoO$_9$, and Sr$_6$Co$_5$O$_{15}$: the influence of transition metal coordination. *J. Phys. Chem. C* **2013**, *117*, 25926.

(22) Liang, H.; Hong, Y.; Zhu, C.; Li, S.; Chen, Y.; Liu, Z.; Ye, D. Influence of partial Mn-substitution on surface oxygen species of LaCoO$_3$ catalysts. *Catal. Today* **2013**, *201*, 98.

(23) Wang, H.; Wu, J.; Dolocan, A.; Li, Y.; Lü, X.; Wu, N.; Park, K.; Xin, S.; Lei, M.; Yang, W.; Goodenough, J. B. Short O−O separation in layered oxide Na$_{0.67}$CoO$_2$ enables an ultrafast oxygen evolution reaction; enables an ultrafast oxygen evolution reaction. *Proc. Natl. Acad. Sci. U.S.A.* **2019**, *116*, 23473.

(24) Xiao, Z.; Huang, Y.-C.; Dong, C.-L.; Xie, C.; Liu, Z.; Du, S.; chen, w.; Yan, D.; Tao, L.; Shu, Z.; Zhang, G.; Duan, H.; Wang, Y.; Zou, Y.; Chen, R.; Wang, S. Operando identification of the dynamic behavior of oxygen vacancy-rich Co$_3$O$_4$ for oxygen evolution reaction. *J. Am. Chem. Soc.* **2020**, *142*, 12087.

(25) Lyu, Y.; Zheng, J.; Xiao, Z.; Zhao, S.; Jiang, S. P.; Wang, S. Identifying the intrinsic relationship between the restructured oxide layer and oxygen evolution reaction performance on the Cobalt Pnictide catalyst. *Small* **2020**, *16*, No. 1906867.

(26) Song, S.; Mao, J.; Shuai, J.; Zhu, H.; Ren, Z.; Saparamadu, U.; Tang, Z.; Wang, B.; Ren, Z. Study on anisotropy of n-type Mg3Sb2-

based thermoelectric materials. *Appl. Phys. Lett.* **2018**, *112*, No. 092103.

(27) Kehne, P.; Guhl, C.; Ma, Q.; Tietz, F.; Alff, L.; Hausbrand, R.; Komissinskiy, P. Electrochemical performance of all-solid-state sodium-ion model cells with crystalline Na$_x$CoO$_2$ thin-film cathodes. *J. Electrochem. Soc.* **2019**, *166*, A5328.

(28) Grimaud, A.; Diaz-Morales, O.; Han, B.; Hong, W. T.; Lee, Y.-L.; Giordano, L.; Stoerzinger, K. A.; Koper, M. T. M.; Shao-Horn, Y. Activating lattice oxygen redox reactions in metal oxides to catalyse oxygen evolution. *Nat. Chem.* **2017**, *9*, 457.

(29) Duan, Y.; Sun, S.; Xi, S.; Ren, X.; Zhou, Y.; Zhang, G.; Yang, H.; Du, Y.; Xu, Z. J. Tailoring the Co 3d-O 2p covalency in LaCoO$_3$ by Fe substitution to promote oxygen evolution reaction. *Chem. Mater.* **2017**, *29*, 10534.

(30) Asnavandi, M.; Yin, Y.; Li, Y.; Sun, C.; Zhao, C. Promoting oxygen evolution reactions through introduction of oxygen vacancies to benchmark NiFe−OOH Catalysts. *ACS Energy Lett.* **2018**, *3*, 1515.

(31) Frost, D. C.; McDowell, C. A.; Woolsey, I. S. X-ray photoelectron spectra of cobalt compounds. *Mol. Phys.* **1974**, *27*, 1473.

(32) Chen, Z.; Wang, J.; Chao, D.; Baikie, T.; Bai, L.; Chen, S.; Zhao, Y.; Sum, T. C.; Lin, J.; Shen, Z. Hierarchical porous LiNi$_{1/3}$Co$_{1/3}$Mn$_{1/3}$O$_2$ nano-/micro spherical cathode material: minimized cation mixing and improved Li$^+$ mobility for enhanced electrochemical performance. *Sci. Rep.* **2016**, *6*, No. 25771.

(33) Perera, J. S. H. Q.; Frost, D. C.; McDowell, C. A. X-ray photoelectron spectroscopy of Co(II), Ni(II), and Cu(II) acetylacetonate vapors. *J. Chem. Phys.* **1980**, *72*, 5151.

(34) Asnavandi, M.; Yin, Y.; Li, Y.; Sun, C.; Zhao, C. Promoting oxygen evolution reactions through introduction of oxygen vacancies to benchmark NiFe−OOH catalysts. *ACS Energy Lett.* **2018**, *3*, 1515.

(35) Zhou, J.; Zhang, L.; Huang, Y.-C.; Dong, C.-L.; Lin, H.-J.; Chen, C.-T.; Tjeng, L. H.; Hu, Z. Voltage- and time-dependent valence state transition in cobalt oxide catalysts during the oxygen evolution reaction. *Nat. Commun.* **2020**, *11*, No. 1984.

(36) Zhuang, L.; Ge, L.; Yang, Y.; Li, M.; Jia, Y.; Yao, X.; Zhu, Z. Ultrathin iron-cobalt oxide nanosheets with abundant oxygen vacancies for the oxygen evolution reaction. *Adv. Mater.* **2017**, *29*, No. 1606793.

(37) Lakshmanan, R.; Gangulibabu; Bhuvaneswari, D.; Kalaiselvi, N. Temperature dependent surface morphology and lithium diffusion kinetics of LiCoO$_2$ cathode. *Met. Mater. Int.* **2012**, *18*, 249.

(38) Castro-García, S.; Sánchez-Andújar, M.; Rey-Cabezudo, C.; Señarís-Rodríguez, M. A.; Julien, C. IR characterization of Ln$_{2-x}$Sr$_x$CoO$_4$ (x≥1; Ln=La, Nd) oxides. *J. Alloys Comd.* **2001**, *323−324*, 710−713.

(39) Zhang, M.; de Respinis, M.; Frei, H. Time-resolved observations of water oxidation intermediates on a cobalt oxide nanoparticle catalyst. *Nat. Chem.* **2014**, *6*, 362.

(40) Gerken, J. B.; McAlpin, J. G.; Chen, J. Y. C.; Rigsby, M. L.; Casey, W. H.; Britt, R. D.; Stahl, S. S. Electrochemical water oxidation with cobalt-based electrocatalysts from pH 0−14: the thermodynamic basis for catalyst structure, stability, and activity. *J. Am. Chem. Soc.* **2011**, *133*, 14431.

(41) Luo, W.; Wang, Y.; Cheng, C. Ru-based electrocatalysts for hydrogen evolution reaction:recent research advances and perspectives. *Mater. Today Phys.* **2020**, *15*, No. 100274.

(42) Wang, Z.; Fan, J.; Cheng, B.; Yu, J.; Xu, J. Nickel-based cocatalysts for photocatalysis: Hydrogen evolution, overall water splitting and CO$_2$ reduction. *Mater. Today Phys.* **2020**, *15*, No. 100279.

(43) Louie, M. W.; Bell, A. T. An investigation of thin-film Ni−Fe oxide catalysts for the electrochemical evolution of oxygen. *J. Am. Chem. Soc.* **2013**, *135*, 12329.

(44) Kuznetsov, D. A.; Han, B.; Yu, Y.; Rao, R. R.; Hwang, J.; Román-Leshkov, Y.; Shao-Horn, Y. Tuning redox transitions via inductive effect in metal oxides and complexes, and implications in oxygen electrocatalysis. *Joule* **2018**, *2*, 225.

(45) Karppinen, M.; Asako, I.; Motohashi, T.; Yamauchi, H. Oxygen nonstoichiometry and actual Co valence in $Na_xCoO_{2-\delta}$. *Phys. Rev. B* **2005**, *71*, No. 092105.

(46) Lee, J. G.; Hwang, J.; Hwang, H. J.; Jeon, O. S.; Jang, J.; Kwon, O.; Lee, Y.; Han, B.; Shul, Y.-G. A new family of perovskite catalysts for oxygen-evolution reaction in alkaline media: $BaNiO_3$ and $BaNi_{0.83}O_{2.5}$. *J. Am. Chem. Soc.* **2016**, *138*, 3541.

(47) Song, S.; Yu, L.; Xiao, X.; Qin, Z.; Zhang, W.; Wang, D.; Bao, J.; Zhou, H.; Zhang, Q.; Chen, S.; Ren, Z. Outstanding oxygen evolution reaction performance of nickel iron selenide/stainless steel mat for water electrolysis. *Mater. Today Phys.* **2020**, *13*, No. 100216.

(48) Xiao, X.; Wang, X.; Li, B.; Jiang, X.; Zhang, Y.; Li, M.; Song, S.; Chen, S.; Wang, M.; Shen, Y.; Ren, Z. Regulating the electronic configuration of ruthenium nanoparticles via coupling cobalt phosphide for hydrogen evolution in alkaline media. *Mater. Today Phys.* **2020**, *12*, No. 100182.

(49) Zhang, L.; Tan, T. T.; Li, S. The effect of annealing oxygen concentration in the transformation of Ca_xCoO_2 to thermoelectric $Ca_3Co_4O_9$. *RSC Adv.* **2015**, *5*, 28158.

(50) Swierk, J. R.; Klaus, S.; Trotochaud, L.; Bell, A. T.; Tilley, T. D. Electrochemical study of the energetics of the oxygen evolution reaction at nickel iron (oxy)hydroxide catalysts. *J. Phys. Chem. C* **2015**, *119*, 19022.

(51) Cowan, A. J.; Barnett, C. J.; Pendlebury, S. R.; Barroso, M.; Sivula, K.; Grätzel, M.; Durrant, J. R.; Klug, D. R. Activation energies for the rate-limiting step in water photooxidation by nanostructured α-Fe_2O_3 and TiO_2. *J. Am. Chem. Soc.* **2011**, *133*, 10134.

(52) Han, J.; Liu, X.; Wan, H.; Wu, D.; Chen, G.; Li, J.; Cao, Y.; Ma, R. Composition tuning of ultrafine cobalt-based spinel nanoparticles for efficient oxygen evolution. *ACS Sustainable Chem. Eng.* **2020**, *8*, 5534.